Review Article

Stefan Röttger*, Ralf Nötzel, Anja Honig, Benoit Sabot and Kerstin Weinberg

Radon sensor networks for large buildings: balancing the trade-off between energy efficiency and health

Radon-Sensornetzwerke für große Gebäude: Abwägung zwischen Energieeffizienz und Gesundheit

https://doi.org/10.1515/teme-2025-0036
Received March 27, 2025; accepted June 21, 2025;
published online July 11, 2025

Abstract: Radon (^{222}Rn) is a radioactive noble gas that is formed in the decay of the primordial ^{238}U decay chain, with an average abundance of 3 parts per million ($3\ \mathrm{g} \cdot \mathrm{t}^{-1}$) in the earth's crust. Since radon is the only noble gas in the decay chain, it has with its half live $T_{\frac{1}{2}} = 3.8232(8)$ d, the ability to emanate from the ground or building materials and to interfere with the biosphere. Taking into account Directive 2013/59/Euratom, the EURAMET EPM project RadonNET was founded to find a trade-off between energy efficiency and health effects by means of measurements with small uncertainties. With this in mind, an pulse ionization chamber for the time-resolved measurement of radon activity at low concentrations is described here. The solution shown is characterized by low sensitivity to room and impact noise. Experimental investigations show the properties of the pulse ionization chamber under various conditions, particularly with regard to its use in sensor networks in larger buildings or future cities.

Keywords: radon; low-level activity concentration; RadonNET; pulse ionization chamber

Zusammenfassung: Radon (^{222}Rn) ist ein radioaktives Edelgas, das beim Zerfall der primordialen ^{238}U-Zerfallsreihe entsteht, das im Erdmantel durchschnittlich mit 3 ppm ($3\ \mathrm{g} \cdot \mathrm{t}^{-1}$) enthalten ist. Da Radon das einzige Gas (sogar Edelgas) in dieser Zerfallskette ist, hat es mit seiner Halbwertszeit $T_{1/2} = 3{,}8232(8)$ d die Möglichkeit, aus dem Erdreich oder Baumaterialien zu emanieren und mit der Biosphäre zu reagieren. Unter Berücksichtigung der Richtlinie 2013/59/Euratom wurde das EURAMET EPM Projekt RadonNET mit dem Ziel gefördert, den Kompromiss zwischen Energieeffizienz (bessere Gebäudehüllenabdichtung) und Gesundheit (stärkere Durchlüftung) durch Messungen mit geringer Unsicherheit zu finden. In diesem Sinne wird hier eine Impulsionisationskammer für die zeitaufgelöste Messung der Radonaktivität bei niedrigen Aktivitätskonzentrationen beschrieben. Die gezeigte Lösung zeichnet sich durch geringe Empfindlichkeit gegenüber Raum- und Trittschall, sowie geringe Kosten aus. Experimentelle Untersuchungen zeigen die Eigenschaften der Impulsionisationskammer unter verschiedenen Bedingungen, insbesondere im Hinblick auf ihren Einsatz in Sensornetzwerken in größeren Gebäudekomplexen.

Schlagwörter: Radon; niederige Aktivitätskonzentrationen; RadonNET; Impulsionisationskammer

1 Introduction

Radon gases and their decay products perform predominantly α-decay and occur in many areas of human life and work. Of natural origin are mainly ^{222}Rn (radon) of the ^{238}U decay chain and ^{220}Rn (thoron) of the ^{232}Th decay chain. Due to the natural distribution of uranium and thorium in the Earth's crust, the radon gases can escape to the surface. Increased activity concentration can be found in the area of ore deposits, e.g., in the Ore Mountains or the Black Forest. The radon is quickly dispersed outdoors, and the measurable activity concentrations are usually only a few Bq m^{-3}. However, there can be a substantial accumulation of several

***Corresponding author: Stefan Röttger**, Physikalisch-Technische Bundesanstalt, Braunschweig, Germany, E-mail: Stefan.Roettger@PTB.de
Ralf Nötzel and Kerstin Weinberg, Lehrstuhl für Festkörpermechanik, Department Maschinenbau, Universität Siegen, 57068 Siegen, Germany, E-mail: Ralf.Noetzel@uni-siegen.de (R. Nötzel), Kerstin.Weinberg@uni-siegen.de (K. Weinberg)
Anja Honig, Physikalisch-Technische Bundesanstalt, Braunschweig, Germany, E-mail: Anja.Honig@PTB.de
Benoit Sabot, Laboratoire National Henri Becquerel (LNE-LNHB), Université Paris-Saclay, CEA, List, F-91120, Palaiseau, France, E-mail: Benoit.SABOT@CEA.fr

100 kBq m^{-3} in buildings, cellars, natural rock crevices, or mining tunnels.

If a human inhales air containing radon, a certain proportion decays into α-emitting decay products, and some of them remain in the lungs. Depending on the activity concentration of the air and the exposure time, this leads to an increased risk of lung cancer. Although these facts have been known for some time, legal regulations for protection against radon have only been in place since the end of 2020 [1].

Therefore, in compliance with the Directive 2013/59/Euratom, member states are required to mitigate ^{222}Rn activity concentration in public and private buildings, where levels regularly exceed the reference threshold of 300 Bq m^{-3}. Authorities are mandated to implement mitigation strategies that adhere to basic safety standards, safeguarding citizens from ionising radiation exposure due to ^{222}Rn progeny. The EURAMET EPM Project RadonNET (23IND07) [2] addresses the challenge of quantifying ^{222}Rn activity concentrations indoors, particularly in large buildings for future cities with a focus on connected, low-energy consumption buildings. The development of methods and sensors for detecting radon activity concentration as well as the creation of quality assured sensor network will enhance on-site ^{222}Rn metrology and provide support to the European radiation protection industry.

1.1 Objectives

Here, the characterization of an adapted pulse ionization chamber for the detection of ^{222}Rn and the α-emitting decay products ^{218}Po, ^{214}Po and ^{210}Po is presented. The technical construction and the electronical features of the detector are explained and a traceable calibration due to national standards is performed which reveal the performance of this detector with regard to the European Council Directive 2013/59/Euratom and the RadonNET project goals.

Two main objectives of RadonNET are to:

1. develop new concepts and methods for sensors detecting radon activity concentration with lowered response time, increased sensitivity and reduced uncertainty compared to existing solutions. To build the sensors in a cost-effective and material-saving way through advanced manufacturing techniques using industrial production by Small and Medium Enterprises (SME),
2. develop traceable, in-situ operando calibration procedures for these sensors with less than 10 % uncertainty at an activity concentration level down to Bq m^{-3}, allowing for response time and dynamic linearity testing.

These goals can be reached with an appropriate transfer standard, as which the here presented detector might serve.

1.2 Detection principles

Several measurement methods have been established for measuring the α-activity in the air:

- PIN diodes and collection of the decay products from ^{222}Rn by means of high voltage on the surface [3],
- Lucas cells with photo multiplier tubes and special sensor technology from e.g. ANSTO [4]–[6],
- Pulse Ionization Chambers with air filling or air flow [7]–[12].

Since the effective surface area of PIN diodes is only a few square centimetres, the α-emitting decay products (^{218}Po, ^{214}Po and ^{210}Po) are collected on the surface by means of an electric field. So-called Lucas cells are combinations of photomultiplier tubes (PMT) and structures coated with zinc sulphide. Each α-decay produces a flash of light, which is counted with the PMT; due to the system, spectroscopy is not possible. In contrast, pulse ionization chambers with air filling allow direct measurement of ^{222}Rn and its decay products as well as α-spectrometry. Such a system is described below.

We note that regardless of the measuring principle, the largest possible active detection volume should be used for the measurement to achieve a low statistical uncertainty within the shortest possible measuring time.

In the following we present a modified pulse ionization chamber for detecting ^{222}Rn and the α-emitting decay products ^{218}Po, ^{214}Po, and ^{210}Po. The basic structure of such pulse ionization chamber is always similar. Two electrodes form a capacitor with air as the dielectric. A high DC voltage in the range of 500 V–2500 V is applied to this capacitor. When an α-particle passes through the air-filled area between the electrodes, the α-particle is slowed down by collisions with oxygen and nitrogen molecules, and the air is ionized. This process produces free charge carriers in the form of positively and negatively charged ions and electrons.

Free ions are then collected on the electrodes and this charge can be detected with a sensitive amplifier. As there is a proportionality between the amount of charge and the energy of the α-particles, a pulse ionization chamber enables an α-spectrometric evaluation of the α-energies.

2 A prototype multiwire pulse ionization chamber

Because the air does not conduct free electrons, these are captured by electronegative oxygen molecules within

around $3 \cdot 10^{-7}$ s. That means that only positive and negative ions remain available as charge carriers. Under the force of the electric field, the free ions drift towards the capacitor electrodes and can be detected as a charge pulse. The drift speed of these ions is relatively low and mainly dependent on the strength of the electric field. Extensive studies were conducted in ref. [13] and could be confirmed selectively by measurements. At a field strength of around 200 V m^{-1}, the ions require around 2 ms–3 ms for a distance of 1 cm. This particular feature must be considered in the mechanical construction and design of the electronic amplifier.

The energy of an α-particle ionizing the air is proportional to the number of ions produced and therefore also proportional to the area of a charge pulse collected from an ionization chamber. Due to the random orientation of an α-particle trajectory in relation to the geometry of the pulse ionization chamber, the maximum charge is variable for the same α-energy.

Earlier investigations were dominated by designs that generated a field strength that was as homogeneous as possible within the pulse ionization chamber. In order to achieve this, relatively thick wires of 0.5 mm up to 2 mm in diameter were used as electrodes and small distances of 1 cm up to 3 cm were chosen between the electrodes [12], [14]. The aim of these measures were to keep the charge carrier collection times of the ions generated by the α-decays as constant and as short as possible. With the same charge carrier collection time, the pulse height of the signals is only dependent on the energy of the α-particles.

Methods originally developed for γ-spectrometry were used for evaluation to enable real-time analysis [15]. In ref. [16], different variants were investigated, and α-energy resolution between 5 % and 10 % were achieved. An analysis of the possibility of improving these results reveals two dominant aspects: Shortened paths of the α-particles and low-frequency, mechanical vibrations caused by room and impact noise during the measurement [16]. Due to the large number and relatively large wire diameter α-particles can collide with the wires before the α-energy can be fully converted into ionized charge carriers. This results in many pulses with lower energy in the spectrum. Under the effect of sound waves, the distance between the plates or wires of the charged capacitor of the pulse ionization chamber changes. This leads to changes in capacitance and voltage pulses as interference. Unfortunately, the frequency spectrum of the electrical pulses, the mechanical natural frequencies of the pulse ionization chamber, and the electrical interference from the 50 Hz power grid are in the same range.

The pulse ionization chamber used here takes a different approach, following the ideas of refs. [7], [8]. Internal construction materials within the trajectories are minimized as far as possible, and the distances between the electrodes were chosen to create an undisturbed trajectory for most α-decays. Depending on the energy of the α-particles, this is between 4 cm and 8 cm in air [17]. Therefore, the α-particles' energy is proportional to the area of the pulses generated. Due to the undetermined orientation of this trajectory in relation to the geometry of the pulse ionization chamber, the maximum value is variable for the same α-energy. To achieve an optimum measurement result, measures must be taken to minimize mechanical and electrical interference and to account for the special features of signal technology.

In refs. [8], [18] a solution is proposed which minimizes the influence of mechanical vibrations. The design of the pulse ionization chamber is coaxial. Two stainless steel tubes with diameters $D_1 = 10$ mm and $D_3 = 168$ mm connected electrically represent one electrode of the capacitor, $D_2 = 64$ mm as a cylindrical construction made of tensioned stainless steel wires (diameter 0.05 mm) represents the second electrode. The total capacitance C_{total} is made up of the calculated areas resulting from the radii ratios D_2/D_1 and D_3/D_2

$$\begin{aligned} C_{\text{total}} &= C\left(\frac{D_2}{D_1}\right) + C\left(\frac{D_3}{D_2}\right) \\ &= 2\pi\varepsilon_0\varepsilon_r l\left(\frac{1}{\ln(D_2/D_1)} + \frac{1}{\ln(D_3/D_2)}\right) \end{aligned} \tag{1}$$

Here ε_0 and ε_r denote the absolute and relative permittivity, and $l = 370$ mm is the working length of the sensor.

If the tensioned wires of D_2 move, the distances and therefore the partial capacitances change in opposite directions. One partial capacitance decreases, while the second partial capacitance increases. Setting up the equilibrium condition

$$C\left(\frac{D_2}{D_1}\right) = C\left(\frac{D_3}{D_2}\right) \tag{2}$$

results in a complete compensation of the capacitance changes. This measure achieves very good damping of the pulse ionization chamber against mechanical vibrations. The equilibrium condition leads to

$$D_2 = \sqrt{D_3 \cdot D_1} \tag{3}$$

For the design of our pulse ionization chamber the following dimensions were selected: $D_1 = 10$ mm, $D_2 = 64$ mm and $D_3 = 168$ mm. With a length of $l = 370$ mm, the effective chamber volume results to 7.7 L. Figure 1 shows the realized pulse ionization chamber as a CAD cut.

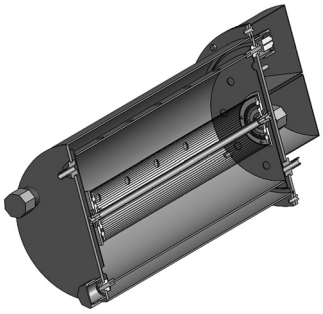

Figure 1: CAD drawing, showing a cut through the pulse ionization chamber. The length of the electrodes is 370 mm and the inner diameter of the outer electrode is 168 mm.

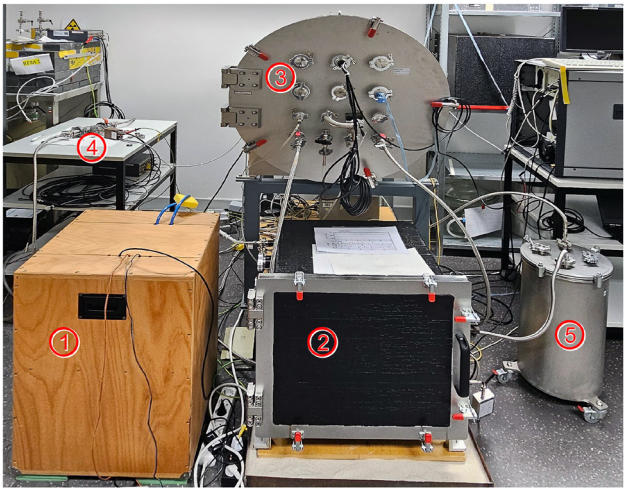

Figure 2: This picture shows the dedicated calibration setup for the pulse ionization chamber. The different components shown are given in the text.

As a further measure, the pulse ionization chamber was installed in a stable wooden box (Figure 2). Two tubes for air inlet and outlet were connected to the pulse ionization chamber and guided through the wooden box. The box is glued to the inside with a layer of 18 mm thick, high-density plasterboard and placed on coordinated elastomer buffers made of polymeric foam of the type Regufoam vibration 150 [19]. All in all, these measures lead to an extraordinarily good suppression of room and impact sound.

The resulting electrical signals are very small and lie in the range of around 100 µV. To suppress any electromagnetic influences, the system is surrounded by an electrically conductive sheath. This is earthed with a low resistance. It is recommended to ensure that no electrical equalizing currents flow through this earth connection. The charge amplifier largely corresponds to the design according to ref. [14]. A low-noise field-effect transistor of type BF862 amplifies the resulting pulse. The dimensioning must be adapted as optimally as possible to the existing conditions of the pulse ionization chamber by means of optimisation. This means that the discharge resistance must be adapted to the statistical mean value of the charge carrier collection time. Thus the following condition to the charge carrier collection time τ must be fulfilled:

$$\tau_{\mathbf{charge}} = \tau_{\mathbf{discharge}}. \tag{4}$$

In our case, the magnitude of $\tau = 3.5$ ms corresponds to a discharge resistance of $R = 1$ GΩ. The feedback capacitor of the charge amplifier has a value of 10 pF. This value was also determined empirically. After optimization, a voltage signal-to-noise ratio of around 50:1 was achieved with the charge amplifier.

With a subsequent instrumentation amplifier (INA111), the reference ground is decoupled from the charge amplifier and a low-impedance measurement signal is generated. The total voltage amplification is 2000 and this signal is read into the personal computer using a USB sound card. Further processing of the signals is carried out with Matlab [20].

3 Experimental set-up and calibration

To determine the response characteristics of the pulse ionization chamber, a dedicated calibration volume has been setup at the Physikalisch-Technische Bundesanstalt (PTB) within a climate controlled laboratory area. A picture of this setup is shown in Figure 2.

The different components shown in Figure 2 are:

1. Pulse ionization chamber discussed here (CIPIC),
2. Multi-Wire-Pulse-Ionization-Chamber of PTB as comparison (VIIK, see Figure 3),
3. Reference volume for low level radon reference atmospheres (LLRRC),
4. Radon emanation source referred to as Integrated Radon Source Detector (IRSD) [21], with absolute ^{226}Ra activities used between 50 Bq and 200 Bq,
5. Additional delay and silencer volume of the VIIK.

The whole calibration system is hermetically closed to radon. Volumes and connecting tubes are, where ever possible, made from stainless steel with vacuum tight connections. All volumes have been measured with a traceable meter and the assigned uncertainties have been determined according to GUM [22]. The calibration volume includes the volumes ③, all the external detector volumes ①, ②, the additional volumes ⑤, the source containing volume ④ and all connecting tubing. All the air displacing volumes of the devices placed inside were subtracted from this calibration volume. (The air displacing volumes were

Figure 3: Multi-wire-puls-ionization-chamber for large volume radon detectors, designed by PTB [12]. The sensitive volume of the VIIK marked with (2) in Figure 2 is displayed here. The gold plated wires are connected to different electrical potential, to separate and collect the ions formed by α-particles passing through the air. The electrodes are distributed over a diameter of about 250 mm and have a length of 300 mm.

determined mainly by traceable weighing and the density of the respective materials.) The full uncertainty budget of the volume determination resulted in a calibration volume $V_{\text{total}} = 0.6744(15)\ \text{m}^3$. The main relative uncertainty contribution of 99.8 % being assigned to the volume determination of the LLRRC ③.

The ^{222}Rn activity concentration within the calibration volume was homogenised using a membrane pump with a flow rate of about 2 L min^{-1}. The external detectors (CIPIC, VIIK) where supplied with calibration air through another small membrane pump with a flow rate of about 1 L min^{-1}.

The background and leakage of the whole system was tested using synthetic, aged air from a 50 L, 200 10^3 hPa canister at a flow rate of about 5 L min^{-1} controlled by a Bronkhorst mass flow controller.

The background count rate of the CIPIC proved to be in average 5.7(45) counts per 1800 s. The calibration system proved ^{222}Rn tight. Back diffusion or emanation from ^{226}Ra contaminated construction materials are under further investigation e.g., applying low level high resolution γ-spectrometry.

4 Calibration measurements

For the purpose of traceable calibration of the CIPIC and comparison with other radon activity concentration detectors, the signals from the CIPIC were recorded and a separate histogram of counts versus channel, respectively

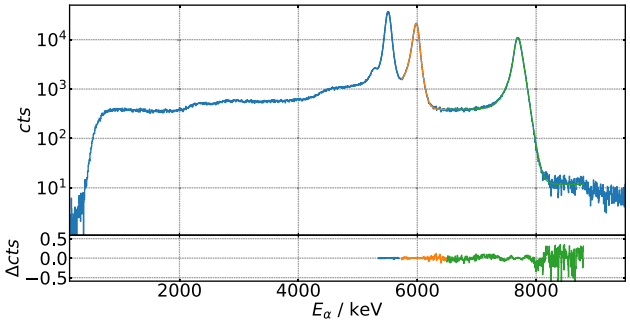

Figure 4: α-spectrum of the CIPIC as histogram of counts over the α-particle-energy. The coloured regions are the fitted regions for ^{222}Rn (blue), ^{218}Po (orange) and ^{214}Po (green). The fit function used is the exponentially modified Gaussian. The lower graph shows the relative residual between the measurements and the fit.

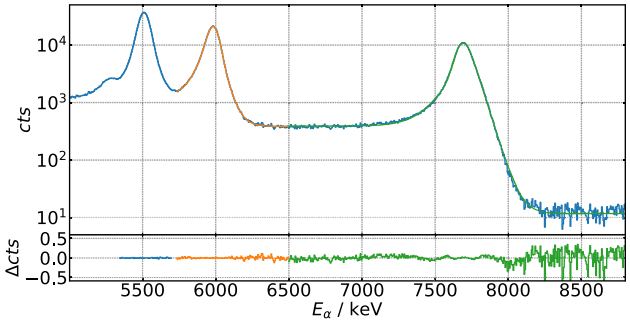

Figure 5: Energy selection of the α-spectrum of the CIPIC as histogram of counts over the α-particle-energy, that contain the peaks found for the α-particle energy of ^{222}Rn (blue) and its progeny ^{218}Po (orange) and ^{214}Po (green). As in Figure 4 an exponentially modified Gaussian with high and low energy tail over a continuous step function is used to determine the area under the peak and the width of the peak and therefore the resolution of the detector.

energy was constructed every 1,800 s (spectrum). To determine the energy resolution of the detector and the shape of the peaks, these spectra where summed up for the duration of the calibration exercise and are shown in Figures 4 and 5. Figure 4 shows the overview of the full energy range of the detector from below 1 MeV up to above 8.5 MeV. The peaks of ^{222}Rn (blue), ^{218}Po (orange) and ^{214}Po (green) are marked. Figure 4 is a cut to the energy range of the isotopes of interest. ^{222}Rn (blue), ^{218}Po (orange) and ^{214}Po (green) are fitted with exponentially modified gaussian peak shapes on top of a smooth step function (sigmoid) as a background.

The resolution of the peaks are:

^{222}Rn: $\sigma = 52.07(4)$ keV at 5489.48(30) keV,
FWHM = 122.6(1) keV, (2.2 %)
^{218}Po: $\sigma = 62.65(6)$ keV at 6002.35(9) keV,
FWHM = 147.5(2) keV, (2.5 %)

^{214}Po: σ = 64.64(9) keV at 7686.82(6) keV,
FWHM = 152.2(3) keV, (2.0 %)

which is an excellent resolution for an air filed pulse ionization chamber at this size of volume. It is more than enough to separate the different isotopes of ^{222}Rn and its progeny. Even ^{210}Po starts to become prominent at 5304.33(7) keV in Figure 5 but is not evaluated so far, due to the delayed production, because of the long half live of ^{210}Pb of $T_{1/2}(^{210}\text{Pb}) = 22.23(12)$ a in the decay chain. The areas under the peaks are used as a measure to determine/calibrate against the ^{222}Rn activity concentration.

4.1 The reference for traceable calibration

The traceable reference to the SI-traceable national reference standard of PTB is given by an active monitored ^{226}Ra source (IRSD) [23] and the corresponding traceable meter for the determination of the volume. The volume for the calibration (LLRRC) is described in Section 3 and shown in Figure 2 as ③. The radium source, which emanates the ^{222}Rn is an implanted Si-diode detectors of Mirion PIPS® series with serial number 41-125F1 with $^{226}RaCl_2$ deposited via thermal-physical vapour deposition (tPVD) directly onto its sensitive surface [24]. The SI-traceable activity of ^{226}Ra determined by the PTB national standard is $A(^{226}\text{Ra}) = 66.4(5)$ Bq.

4.1.1 Determination of the ^{222}Rn reference atmosphere

The stability of the IRSD is monitored during the whole calibration time taking α-particle energy spectra with the IRSD itself using a pre-amplifier of type Ametek Ortec, Model 142B connected to a Mirion Lynx® data acquisition registering 16 k channel spectra every 5000 s. Figure 6 shows a waterfall plot of the spectra collected during this calibration. The x-axis represents the energy of the α-particles in channel compressed by a factor of 2. The y-axis represents the date time the spectrum was stored. The colour codes the number of events recorded for the respective channel. Practically no variation above the single count level can be found during the whole time.

Therefore all spectra are summed up, to determine the best peak shape and fit function for the evaluation of the time series of α-spectra, see Figure 7.

The α-spectra of the IRSD where evaluated fitting the appropriate nuclide α-energy peaks to the measured counts. As a shape of the single peaks an exponentially modified gaussian with several high and low energy tail over a continuous step function (sigmoid) is used with an optimisation process, that prefers similar peak shapes for all peaks

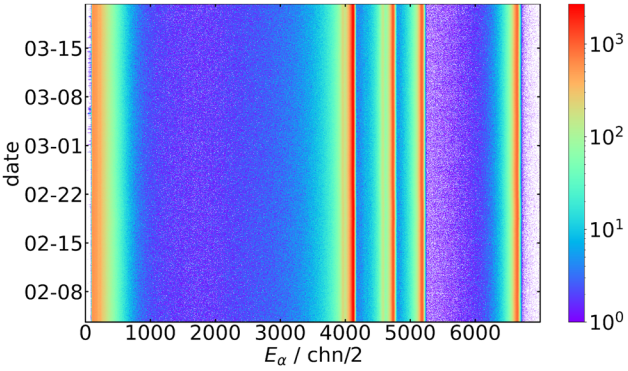

Figure 6: Waterfall plot of the α-spectra acquired with the IRSD during the calibration measurement of the CIPIC. Given is from bottom to top the timely evolution of the α-energy-spectra over the compressed channels showing the counts per channel in colour coding. This kind of figure is used to check the stability of the efficiency and the stability of the detector and amplification of the electronics, which in this case is excellent over such a long time.

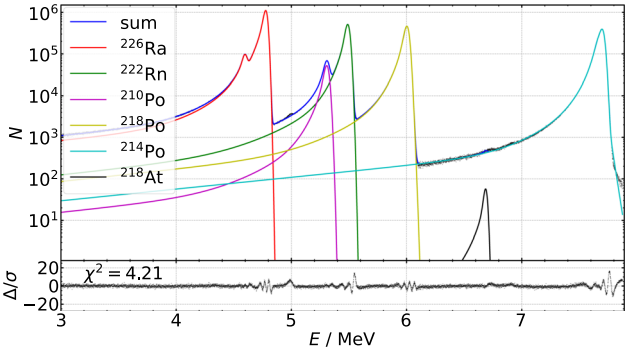

Figure 7: α-energy-spectrum of the IRSD-41-125F1 calibration source with a calibrated ^{226}Ra activity of $A(^{226}\text{Ra}) = 66.4(5)$ Bq against the German national standard. ^{226}Ra and its progeny with their contribution to the peaks are shown in different colours (see legend). The dark blue curve is the sum of all peak areas and is compared with the black dots which are the results of the sum of the measurements of the IRSD. The relative difference between the sum of the peak areas and the measured counts is shown in the residual below. $\chi^2 = 4.21$ is a measure for the goodness of the model and the fit.

but allows for differences adding a penalty function in the loss function of the optimizer for varying shapes. Excellent agreement between model and data is fund as shown in the residuals of Figure 7 with a small $\chi^2 = 4.21$. This shape of the summed α-energy spectrum is then transfered to all the single spectra to produce a time and isotope resolved series of counts which is necessary for the filtering process.

Using this time resolved data it is possible to determine the stability and uncertainty of the IRSD standard.

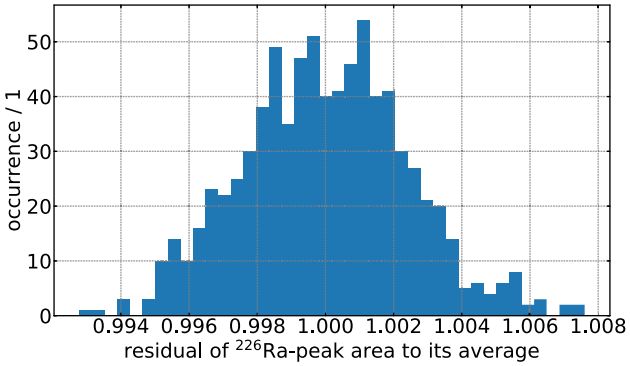

Figure 8: Frequency distribution of the relative difference of the areas of the peak fits for the ^{226}Ra decay energy from the IRSD for the 5000 s interval measurements during the entire calibration exercise is shown in this figure. The residual distribution which is distributed well within ±0.5 % demonstrates the quality, stability and efficiency of the IRSD used even with such low, total activity as $A(^{226}\mathrm{Ra}) = 66.4(5)$ Bq.

Therefore the ^{226}Ra data is used and plotted as histogram of the relative difference between the average and the single values – see Figure 8.

Here the quality, efficiency and stability is demonstrated through a distribution that is well within ±0.5 % for a source with an total activity of only $A(^{226}\mathrm{Ra}) = 66.4(5)$ Bq.

The reference ^{222}Rn activity concentration in the calibration volume in non-steady-state situations is estimated using the Switching Linear Dynamical System (SLDS) deconvolution approach of the observed counts time-series, which is evaluated from the IRSD spectrometric time-series using the methods of the Savitzky Golay Filter [25] for smoothing of the data and regarding the state of the system as stochastic differential equation (SDE) in the It ō sense. Using recursive Bayesian estimation yield to a Kalman-Filter for state-integrating, discretized Gaussian processes, as realised in ref. [21]. The results of the application of such a filtering process on the data collected with the IRSD in the calibration system used, is summarised in Figure 9.

Figure 9 combines the measured and time resolved fitted data of the IRSD represented in the blue dots with the left scale in the second and third row for ^{222}Rn and ^{226}Ra, respectively. The results of the filtering process is given in the first four rows as black line with grey uncertainty areas

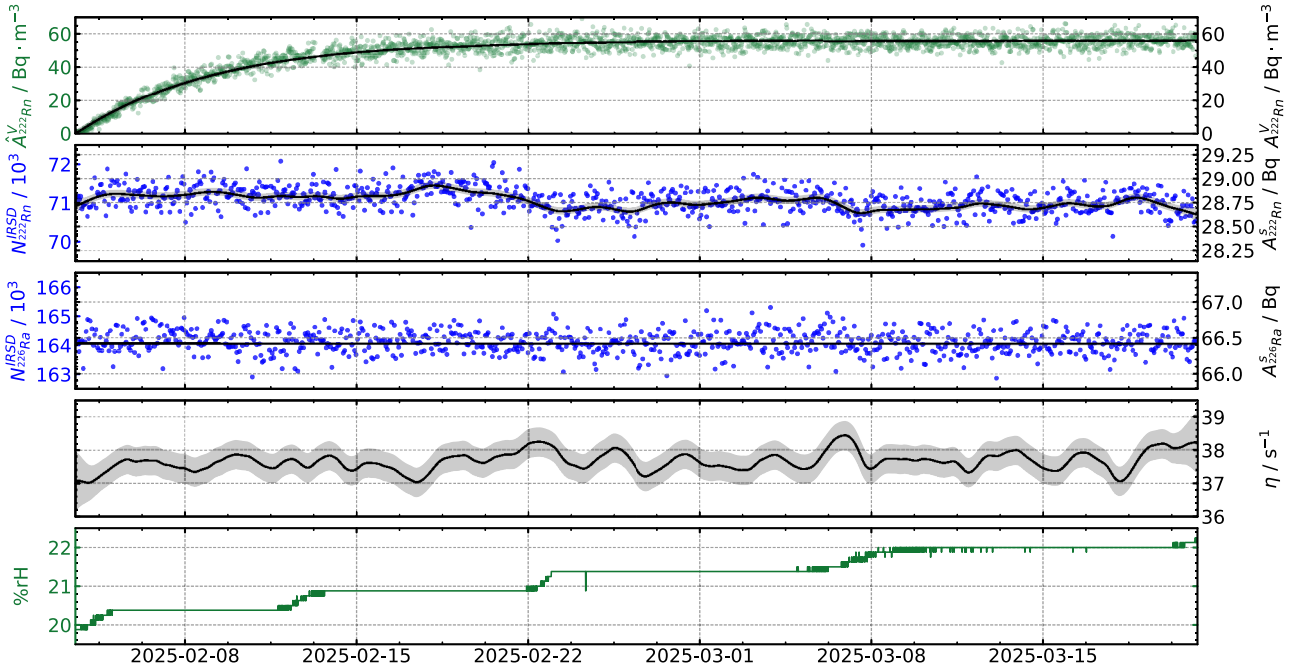

Figure 9: Evaluation of the IRSD measurements using a Kalmann filter system working on the time and energy resolved data generated with the IRSD and pre-evealuated fitting the peak areas of the different nuclides using the fit shown in Figure 7. From top to bottom: the first row shows the comparison of the ^{222}Rn peak area results (green dots) determined over time for 1800 s time intervals calibrated to Bq m^{-3} over time, compared to the results inferred from the IRSD that was used to perform the calibration. The black line represents the value and the grey area the standard uncertainty ($k = 1$) at this point in time and connected to the right axis. The same systematics is used for the upper four rows. The second row shows the peak areas of the ^{222}Rn peaks inferred from the IRSD for 5000 s intervals as blue dots with respect to the left scale. This is compared to the activity of ^{222}Rn measured in the source of the IRSD. The third row shows the same as the second but with respect to ^{226}Ra. The forth row shows calculated number of emanated ^{222}Rn atoms per second from the source of the IRSD. The fifth row shows the relative humidity in the calibration volume LLRRC (recorded with the AlphaGURAD 1950 detector present as a reference instrument during all the calibration) shown here because of the main dependency of the emanation from changing humidity.

($k = 1$) using the right scales. The new result calculated with the filter is the fourth row which shows the released ^{222}Rn atoms per second (η/s^{-1}). This shows some very minor variation but no significant correlation with the main environmental parameter which is the humidity. For comparison the relative humidity is given in the fifth row. And the ^{222}Rn activity concentration during the calibration in the volume which is shown in the first row (A^V_{Rn}/Bq m^{-3}, right scale). The first row compares this absolute traceable reference value with the calibrated measurements from the CIPIC, which is derived from the calibration explained in Section 5.

5 Results

Taking the ^{222}Rn activity concentration determined with the IRSD as reference, it is possible to prepare a correlation plot between the timely synchronised values from the IRSD (on the x-axis) and the corresponding determined ^{222}Rn areas from the peak fits to the spectra Figure 4 (on the y-axis). This plot is shown in Figure 10.

The blue line in Figure 10 is determined via a linear fit to all the data acquired during the calibration. With the help of this calibration plot one can determine the residual distribution of the CIPIC counts areas for ^{222}Rn calibrated to Bq m^{-3} to the linear fit. This distribution is shown in Figure 11.

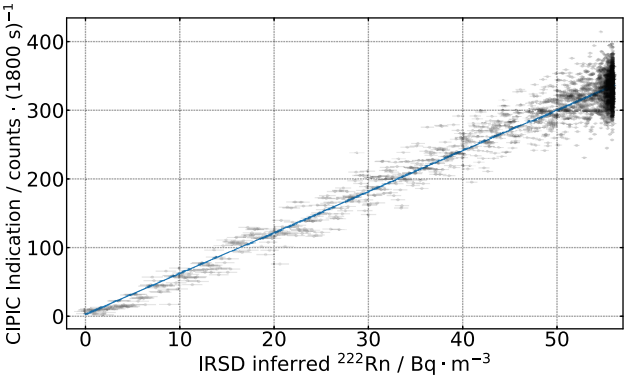

Figure 10: Calibration plot of the single spectra measurements with the CIPIC inferred ^{222}Rn α-peak areas against the inferred results from the α-spectra of the IRSD. The blue line indicates the fitted linear calibration to all data points during the calibration exercise. The distribution of the difference between this determined calibration and the measurement results of the CIPIC is given in Figure 11.

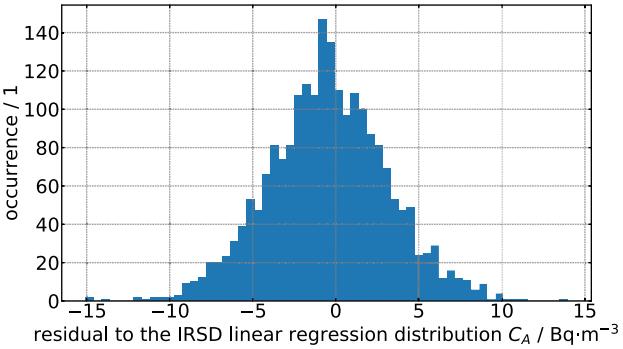

Figure 11: Frequency distribution of the deviation of the CIPIC measurements for the ^{222}Rn α-peak area calibrated to Bq m^{-3} from the calibration determined with the measurement results inferred from the IRSD. The distribution shows a well centred shape with a narrow distribution demonstrating the quality of the CIPIC results.

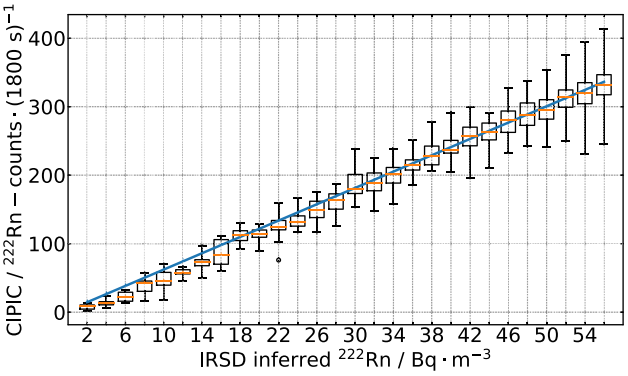

Figure 12: Grouping all the measurements from Figure 10 in equal distances of activity concentration given by the IRSD, a dedicated calibration plot from 2 Bq m^{-3} to 56 Bq m^{-3} is given here as boxed plot showing the uncertainty interval for each group of activity concentration. The stright blue line is the determined calibration which is in good agreement with all determined uncertainty intervals.

It shows a Gaussian shape with an approximate FWHM of about 5 Bq m^{-3}, which is a very good result regarding the activity concentration range which is below 56 Bq m^{-3}.

Grouping of the data allows for a more detailed statistical view on the calibration, which is given in Figure 12, showing the box plot of the calibration.

The so determined linear calibration of the CIPIC is given by the offset of 2.677(9) counts and the linear factor of 5.958(2) counts Bq^{-1}.

All the essential parameters and features of the used pulse ionization camber are combined to Table 1.

Table 1: Summary of the essential parameters and features of the used pulse ionization chamber detector.

Geometrical dimensions:		
Height of the electrodes	370	mm
Diameter of D1	10	mm
Diameter of D2	64	mm
Diameter of D3	168	mm
Outer box height	740	mm
Outer box length	490	mm
Outer box depth	490	mm
Detector features:		
Background count rate during 1800 s	5.7 (45)	cts $(1800\ s)^{-1}$
Linear calibration offset	2.677 (9)	cts
Linear calibration factor	5.958 (2)	cts Bq^{-1}
Full width at half maximum:		
^{222}Rn (5489.48(30) keV)	122.6 (1)	keV (2.2 %)
^{218}Po (6002.35(9) keV)	147.5 (2)	keV (2.5 %)
^{214}Po (7686.82(6) keV)	152.2 (3)	keV (2.0 %)
Statistical std. deviation from linear calibration below 60 Bq m^{-3} within 1800 s integration time	± 5	Bq m^{-3}

6 Summary and perspectives

A new detector based on the principle of an air filled pulse ionization chamber for the measurement of ^{222}Rn activity concentration has been designed, build and characterised. The sensitivity of the detector was selected to be usable from lower indoor air ^{222}Rn activity concentrations down to outdoor air ^{222}Rn activity concentration, as usual in outdoor air in European cities.

This detector is vital for the use in networked sensors in large buildings or future cities, as envisioned, e.g., in the RadonNET project, to balance the trade-off between energy efficiency and health.

Special attention has been paid to the detection system's energy resolution by suppressing the influence of acoustics or vibrations on the detector's operation. With a relative Full Width at Half Maximum of smaller than 3 %, the separation of the signals from ^{222}Rn and its progeny is easily available. The detector is calibrated and traceable to the SI via the national German standard for α-emitting activity sources. In this first calibration exercise, a standard uncertainty for the activity concentration of ± 5 Bq m^{-3} was reached even for activities below 50 Bq m^{-3}, within 1800 s.

Future investigations of the CIPIC will involve reproducibility, linearity, time response, and extended dead time correction. In addition, more detectors of different sizes are under production for dedicated indoor or outdoor use. The materials used for the construction of the detector are under investigation concerning ^{226}Ra contamination and, therefore, an emanation of ^{222}Rn, as well as ^{222}Rn diffusion and leakage.

Acknowledgments: The autors gratefully acknowledge the support of the 23IND07 RadonNET project 'Radon metrology: Sensor networks for large buildings and future cities'. RN and KW gratefully acknowledge the support provided by the workshops of the University of Siegen.

Research ethics: Not applicable.

Informed consent: Not applicable.

Author contributions: All authors have accepted responsibility for the entire content of this manuscript and approved its submission.

Use of Large Language Models, AI and Machine Learning Tools: None declared.

Conflict of interest: All other authors state no conflict of interest.

Research funding: The project 23IND07 RadonNET has received funding from the European Partnership on Metrology, co-financed from the European Union's Horizon Europe Research and Innovation Programme and by the Participating States.

Data availability: The raw data can be obtained on request from the corresponding author.

References

[1] BfS, "Legal regulations for the protection against radon," 2024. https://www.bfs.de/EN/topics/ion/environment/radon/regulations/law.html [accessed: Mar. 05, 2025].

[2] EURAMET, "Partnership on metrology, radon metrology: sensor networks for large buildings and future cities (RadonNET)," 2023. https://radon-network.eu [accessed: Jun. 18, 2025].

[3] G. Pronost, M. Ikeda, T. Nakamura, H. Sekiya, and S. Tasaka, "Development of new radon monitoring systems in the kamioka mine," *Prog. Theor. Exp. Phys.*, vol. 2019, no. 7, p. 079201, 2019.

[4] S. D. Chambers, *et al*., "Characterizing atmospheric transport pathways to Antarctica and the remote southern ocean using radon-222," *Front. Earth Sci.*, vol. 6, p. 190, 2018.

[5] S. Whittlestone, W. Zahorowski, and P. Wasiolek, *High Sensitivity Two Filter Radon/Thoron Detectors with a Wire or Nylon Screen as a Second Filter*, ANSTO, 1994. https://apo.ansto.gov.au/server/api/core/bitstreams/aeb3b687-ed4c-76a5-e053-150a9d89ded9/content [accessed: Jun. 17, 2025].

[6] A. G. Williams and S. D. Chambers, *A History of Radon Measurements at Cape Grim*, ANSTO, 2016, Australian Nuclear Science and Technology Organisation, Kirrawee DC, NSW1 This article has been reproduced from Baseline Atmospheric Program (Australia), 2011—2013.

[7] R. A. Etezov, *et al*., "^{222}Rn content variations at ground and underground conditions," 2022. arXiv:2110.15289.

[8] Y. M. Gavrilyuk, A. M. Gangapshev, V. V. Kuzminov, S. I. Panasenko, and S. S. Ratkevich, "Monitoring the ^{222}Rn concentration in the air of low-background laboratories by means of an ion-pulse ionization chamber," *Bull. Russ. Acad. Sci. Phys.*, vol. 75, no. 4, pp. 547—551, 2011.

[9] Y. M. Gavrilyuk, *et al*., "High-resolution ion pulse ionization chamber with air filling for the ^{222}Rn decays detection," *Nucl. Instrum. Methods Phys. Res. Sect. A Accel. Spectrom. Detect. Assoc. Equip.*, vol. 801, pp. 27—33, 2015.

[10] A. Hartmann, J. Hutsch, F. Krüger, M. Sobiella, H. Wilsenach, and K. Zuber, "Design and performance of an ionisation chamber for the measurement of low alpha-activities," *Nucl. Instrum. Methods Phys. Res. Sect. A Accel. Spectrom. Detect. Assoc. Equip.*, vol. 814, no. 1, pp. 12—18, 2016.

[11] V. V. Kuzminov, "Ion-pulse ionization chamber for direct measurement of radon concentration in the air," *Phys. Atom. Nucl.*, vol. 66, no. 3, pp. 462—465, 2003.

[12] S. Röttger, A. Paul, A. Honig, and U. Keyser, "On-line low- and medium-level measurements of the radon activity concentration," *Nucl. Instrum. Methods Phys. Res. Sect. A Accel. Spectrom. Detect. Assoc. Equip.*, vol. 466, no. 3, pp. 475—481, 2001.

[13] M. Esmaeili-Sanjavanmareh, M. Sohrabi, and M. Habibi, "Optimizing some parameters of air-filled ion pulse ionization chambers for effective radon detection," *Appl. Radiat. Isot.*, vol. 199, no. 110870, 2023.

[14] D. Linzmaier, *Entwicklung einer Low-Level-Radon-Referenzkammer*, Ph.D. thesis, Gottfried Wilhelm Leibniz Universität Hannover, 2013. Available at: https://repo.uni-hannover.de/handle/123456789/8171.

[15] M. Lauer, *Digital Signal Processing for Segmented HPGe Detectors Preprocessing Algorithms and Pulse Shape Analysis*, Heidelberger Dokumentenserver, 2004. Available at: https://archiv.ub.uni-heidelberg.de/volltextserver/4991/ [accessed: Jul. 01, 2025].

[16] D. Linzmaier and A. Röttger, "Development of a low-level radon reference atmosphere," *Appl. Radiat. Isot.*, vol. 81, pp. 208—211, 2013.

[17] M. Dehnert, "Radioaktivität und Dosimetrie" Alpha-protect-Strahlung," 2025. https://www.tu-chemnitz.de/physik/FPRAK/FPI/Versuche_alt/valpha.pdf [accessed: Mar. 05, 2025].

[18] R. Nötzel and K. Weinberg, "Design of a high-resolution ion pulse ionization chamber for 222rn decays detection in air," subm. to: *Nucl. Instrum. Methods Phys. Res. Sect. A Accel. Spectrom. Detect. Assoc. Equip.*, 2025.

[19] Berleburger Schaumstoffwerke GmbH, "Regufoam schwingungstechnik technische daten," 2024. Release 6. http://www.bsw-schwingungstechnik.de [accessed: Jun. 17, 2025].

[20] Matlab, 2025. https://de.mathworks.com/products/matlab.html [accessed: Mar. 5, 2025].

[21] F. Mertes, "Primary ^{222}Rn emanation standards for low-level applications," 2023. Available at: https://repo.uni-hannover.de/handle/123456789/15493.

[22] BIPM, IEC, IFCC, ILAC, ISO, IUPAC, IUPAP, and OIML, "Evaluation of measurement data — guide to the expression of uncertainty in measurement," Joint Committee for Guides in Metrology, JCGM 100, 2008.

[23] F. Mertes, S. Röttger, and A. Röttger, "Approximate sequential bayesian filtering to estimate ^{222}Rn emanation from ^{226}Ra sources using spectral time series," *J. Sens. Sens. Syst.*, vol. 12, no. 2, pp. 147—161, 2023.

[24] S. Röttger, A. Röttger, F. Mertes, V. Morosch, T. Ballé, and S. Chambers, "Evolution of traceable radon emanation sources from MBq to few Bq," *Appl. Radiat. Isot.*, vol. 196, p. 110726, 2023.

[25] A. Savitzky and M. J. E. Golay, "Smoothing and differentiation of data by simplified least squares procedures," *Anal. Chem.*, vol. 36, no. 8, pp. 1627—1639, 1964.